

Polycyclic Aromatic Hydrocarbon and Emission Line Ratios in Active Galactic Nuclei and Starburst Galaxies.

Dinalva A. Sales¹; M. G. Pastoriza^{1,2} and R. Riffel¹
 dinalva.aires@ufrgs.br; pastoriza@ufrgs.br; riffel@ufrgs.br

ABSTRACT

We study the polycyclic aromatic hydrocarbons (PAH) bands, ionic emission lines, and mid-infrared continuum properties, in a sample of 171 emission line galaxies taken from the literature plus 15 new active galactic nucleus (AGN) *Spitzer* spectra. We normalize the spectra at $\lambda = 23\mu\text{m}$ and grouped them according to the type of nuclear activity. The continuum shape steeply rises for longer wavelengths and can be fitted with a warm blackbody distribution of $T \sim 150\text{--}300\text{K}$. The brightest PAH spectral bands (6.2, 7.7, 8.6, 11.3, and $12.7\mu\text{m}$) and the forbidden emission lines of [Si II] $34.8\mu\text{m}$, [Ar II] $6.9\mu\text{m}$, [S III] 18.7 and $33.4\mu\text{m}$ were detected in all the starbursts and in $\sim 80\%$ of the Seyfert 2. Taking under consideration only the PAH bands at $7.7\mu\text{m}$, $11.3\mu\text{m}$, and $12.7\mu\text{m}$ we find that they are present in $\sim 80\%$ of the Seyfert 1, while only half of this type of activity show the $6.2\mu\text{m}$ and $8.6\mu\text{m}$ PAH bands. The observed intensity ratios for neutral and ionized PAHs ($6.2\mu\text{m}/7.7\mu\text{m} \times 11.3\mu\text{m}/7.7\mu\text{m}$) were compared to theoretical intensity ratios, showing that AGNs have higher ionization fraction and larger PAH molecules (≥ 180 carbon atoms) than SB galaxies. The ratio between the ionized ($7.7\mu\text{m}$) and the neutral PAH bands ($8.6\mu\text{m}$ and $11.3\mu\text{m}$) are distributed over different ranges for AGNs and SB galaxies, suggesting that these ratios could depend on the ionization fraction, as well as on the hardness of the radiation field. The ratio between the $7.7\mu\text{m}$ and $11.3\mu\text{m}$ bands is nearly constant with the increase of $[\text{Ne III}]15.5\mu\text{m}/[\text{Ne II}] 12.8\mu\text{m}$, indicating that the fraction of ionized to neutral PAH bands does not depend on the hardness of the radiation field. The equivalent width of both PAH features show the same dependence (strongly decreasing) with $[\text{Ne III}]/[\text{Ne II}]$, suggesting that the PAH molecules, emitting either ionized ($7.7\mu\text{m}$) or neutral ($11.3\mu\text{m}$) bands, may be destroyed with the increase of the hardness of the radiation field.

Subject headings: galaxies: Seyfert – galaxies: starburst – infrared: ISM – ISM: molecules – techniques: spectroscopic

1. Introduction

The Mid-infrared (Mid-IR) spectra of galaxies either with active nucleus (AGN) and/or Starburst (SB) show emission features attributed to Polycyclic Aromatic Hydrocarbons (PAH), which can be considered to be originated in very small amorphous carbon dust grains or very large

carbon-rich ring molecules (e.g. Puget & Leger 1989; Draine & Lee 1984; Draine & Li 2001). The most prominent, well-known PAH emissions, are the $6.2\mu\text{m}$, $7.7\mu\text{m}$, $8.6\mu\text{m}$, $11.2\mu\text{m}$ and $12.7\mu\text{m}$ bands (e.g. Roche et al. 1991; Genzel et al. 1998; Weedman et al. 2005; Buchanan et al. 2006). Besides, the Mid-IR spectral region also presents prominent forbidden ionic emission lines, such as [Ne II] $12.8\mu\text{m}$, [Ne V] $14.3\mu\text{m}$, [Ne III] $15.5\mu\text{m}$, [S III] $18.7\mu\text{m}$ and $33.48\mu\text{m}$, [O IV] $25.89\mu\text{m}$ and [Si II] $34.8\mu\text{m}$ (e.g. Sturm et al. 2002; Bernard-Salas et al. 2009).

The nature of the ionizing source can be as-

¹Departamento de Astronomia, Universidade Federal do Rio Grande do Sul. Av. Bento Gonçalves 9500, Porto Alegre, RS, Brazil

²Conselho Nacional de Desenvolvimento Científico e Tecnológico, Brazil

essed by computing the intensity ratios between forbidden lines such as [Ne II] $12.8\mu\text{m}$, [Ne III] $15.5\mu\text{m}$ and [Ne V] $14.3\mu\text{m}$ (e.g. Voit 1992). In addition, the detection of [Ne V] at $14.3\mu\text{m}$ and $24.2\mu\text{m}$ or [Ne VI] at $7.6\mu\text{m}$, due to ions of high ionization potential, is an evidence of a hard radiation field associated with an AGN (Genzel et al. 1998; Sturm et al. 2000).

Several diagnostic diagrams based on the line intensity ratios between the brightest ionic lines and the PAH features have been proposed to classify the Mid-IR spectra of galaxies according to the degree of activity (AGN, low-ionization nuclear emission-line region - LINER, and SB galaxies). For instance, Genzel et al. (1998), using data from the Short Wavelength Spectrometer (SWS) on board of the Infrared Space Observatory (ISO), propose the diagnostic diagram, [O IV] $25.9\mu\text{m}$ /[Ne II] $12.8\mu\text{m}$ versus the strength of the $7.7\mu\text{m}$ PAH band to separate star-forming galaxies from AGNs.

From the study of the Mid-IR spectra of quiescent spirals, Galactic HII regions, planetary nebulae, and photodissociation regions (PDRs), Galliano (2006) found that the ratios between the $6.2\mu\text{m}/8.6\mu\text{m}$ and $7.7\mu\text{m}/8.6\mu\text{m}$ PAH bands do not vary significantly, while the ratios $6.2\mu\text{m}/11.3\mu\text{m}$ and $7.7\mu\text{m}/11.3\mu\text{m}$ varies over one order of magnitude. They concluded that the properties of the PAHs for different types of galaxies are very similar and that variations of the PAH band ratios are due to the fraction of ionized to neutral PAH molecules. Thus, this ratio could be used to analyze the physical conditions of the molecular gas in the regions where the emission is originated. In addition, Gordon et al. (2008) found that the equivalent width (EW) of PAH features, observed in HII regions of the M101 galaxy are correlated with the ionization index, and does not depend on the HII regions metallicity.

According to Smith et al. (2007) the ionized to neutral fraction of PAHs can be estimated using PAH $7.7\mu\text{m}/11.3\mu\text{m}$ ratio, which is sensitive to the type of nuclear activity, decreasing from SB to Seyfert. These authors, suggest that this behavior is due to the selective destruction of the $7.7\mu\text{m}$ PAH molecule with the increasing hardness of the radiation field (similar results are found by O'Dowd et al. 2009; Hunt et al. 2010; Kaneda et al. 2008). Such results are supported

by laboratory experiments, which show that certain PAHs are effectively destroyed by individual UV and X-ray photons, and cannot survive within a few kiloparsecs from an active nucleus, unless they are shielded from the AGN's X-ray emission by absorbing material (Voit 1992).

It is worth mentioning that the above results, concerning the ionization fraction of PAH bands in AGNs are carried out with small samples of this type of object. Therefore, we use the largest sample of AGNs and SB galaxies available up to date in Spitzer public archive, to study in detail the effect of the hardness of the radiation field on the PAH bands emission, in these kind of galaxies. This paper is structured as follows: in Sect. 2 we describe the sample selection, data reduction process and emission line measurements. In Sect. 3 we present results and discussions on the shape of the continuum spectra, emission line frequency and diagnostic diagrams of PAH band ratios and emission lines ratios. Sect. 4 we discuss the behavior of the ionization fraction and EW of PAH bands with the hardness of radiation field. Summary and conclusion are presented in Sect. 5.

2. The Sample

We have analyzed a well defined sample of 186 galaxies which have Spitzer spectra available from public archive. Being 83 AGNs taken from Gallimore et al. (2010), 22 SB from (Brandl et al. 2006), 59 HII and LINER from (Smith et al. 2007) and 7 HII regions of M101 galaxy from (Gordon et al. 2008), plus 15 AGNs Spitzer spectra published here for the first time. Details on the reduction process of the 15 new objects are given below.

2.1. Data Reduction

The 15 new spectra of AGN galaxies (4 Sy 1 and 11 Sy 2) were obtained from the Spitzer public archive. Observations were performed with the Infrared Spectrograph (IRS; Houck et al. 2004) using the Short-Low (SL) and Long-Low (LL) modules, covering the interval between $5\mu\text{m}$ and $36\mu\text{m}$ with a resolving power of 64 - 128. The raw data were processed using the Spitzer PIPELINE version 17.2¹. The nuclear spectra were extracted using

¹Available at: <http://ssc.spitzer.caltech.edu/spitzerdataarchives/>

the Spitzer IRS Custom Extractor - SPICE². Default point-source extractions were selected for all objects. Only a few sources show a noticeable step in flux between the overlapping LL and LS module spectra, which results from the extended circumnuclear emission contribution to the size SL module slit of $3''.7 \times 57''$ and LL module slit of $10''.7 \times 168''$. Although the observed regions of almost all of the galaxies are large in both modules the AGN light dominates the spectra. Fig. 1 shows the emission spatial profile of NGC3786. Note that the luminosity falls off to almost zero for ≈ 3 pixels from the center of the nucleus. For this galaxy, 3 pixels correspond to ≈ 1 kpc, adopting a radial velocity of 2678 km sec^{-1} and a Hubble constant of $74 \text{ km sec}^{-1}\text{Mpc}^{-1}$.

The general parameters for the objects listed in Table 1 were taken from NASA/IPAC Extragalactic Database (NED). All the spectra were corrected for redshift. The rest-frame spectra were grouped according to their activity, and are shown in Fig. 2.

2.2. Emission Line Measurements

For the 15 new AGNs listed in the Table 1 and SB taken from Brandl et al. (2006), low resolution IRS spectra have been decomposed using the PAHFIT³ code, described in detail by Smith et al. (2007). In short, they assume that the IRS spectra are composed by dust continuum, starlight, prominent emission lines, individual and blended PAH emission bands, and that the light is attenuated by extinction due to silicate grains.

The default input parameters of PAHFIT are: (i) the infrared emission from a blackbody with $T=5000 \text{ K}$; (ii) different weights for thermal dust continuum components represented by the temperatures 35, 40, 50, 90, 135, 200, 300K; (iii) spectral line features, including the pure rotational lines of the molecular hydrogen; (iv) dust features are represented by individual and blended Drude profiles, which are theoretical frequency profiles for a classical damped harmonic oscillator and are the best choice to model PAH emission. For more details see Smith et al. (2007).

With the above constraints we were able to iso-

late the PAH features and measure their fluxes, as well as those of the ionized gas emission lines. The fluxes and the EW are listed in Tables 2 to 3. We checked the consistency of the results with the LINER code (Pogge & Owen 1993) that integrates the flux of a Gaussian function fitted to the line, obtaining similar results in both procedures. The observed IRS spectra of Mrk334, a Sy 1 galaxy, is shown in Fig. 4, where we also plot the detailed components of the PAHFIT spectral decomposition model. Clearly, the model reproduces well the observed spectrum.

3. Results and Discussion

3.1. New spectra

The main goal of this section is to characterize the continuum shapes and spectral features observed in the 15 new objects listed in Table 1, with respect to the type of nuclear activity (Sy 1 and Sy 2). Therefore, we normalize to unity the continuum of all spectra at $\lambda = 23 \mu\text{m}$ and grouped them according to nuclear activity. For each AGN class, data were sorted according to spectral shape, from bluest to reddest, top to bottom of Fig. 2, respectively. One can clearly see that the majority of spectra have a continuum shape increasing for longer wavelengths, in agreement with results found by Weedman et al. (2005); Buchanan et al. (2006); Deo et al. (2009); Burtscher et al. (2009); Wu et al. (2009); Baum et al. (2010). This continuum range can be fitted with a warm blackbody distribution of $T \sim 150 - 300 \text{ K}$. Interestingly, a similar trend in the continuum of AGNs is also observed in the near-infrared region (Riffel et al. 2006; Riffel et al. 2009).

We compare the spectroscopic properties of the 15 new objects with those of the Buchanan et al. (2006) groups. We found that the spectra of the Sy 2 galaxies: NGC3786, NGC5728, NGC7682, Mrk471, Mrk609, Mrk622, Mrk883, Mrk1066, Mrk883 and the Sy 1 Mrk334 and NGC4748, have the same characteristic as their group 1 (strong PAH emission and red continuum, see Fig 2). On the other hand the Sy 2, NGC 1275, NGC2622, Mrk3 and Sy 1 Mrk 478 can be classified as group 3 (power-law continuum and weak PAH features), while only the Sy 1 Mrk279 galaxy show a broken continuum and silicate emission at $9.8\mu\text{m}$ (group

²Available at: <http://ssc.spitzer.caltech.edu/postbcd/spice.html>.

³Source code and documentation for PAHFIT are available in <http://tir.astro.utoledo.edu/jdsmith/research/pahfit.php>

2). In summary, for our and Buchanan et al. (2006) samples the Mid-IR spectra for most of Sy 2 galaxies have same spectroscopic characteristics as those of group 1 (> 50%).

3.2. PAH and Emission Line Frequency

Fig. 3 shows a histogram of the commonest emission features present in each type of activity (note that we have used the 186 galaxies spectra). It is clear from this figure that the PAH features are present in almost all the Sy 1, Sy 2 and SB galaxies, as well as the H₂ molecules at 9.6 μ m and 17 μ m. In addition, the most frequent ionic lines are: [Si II] 34.8 μ m, [Ar II] 6.9 μ m, [S III] 18.7 and 33.4 μ m, [S IV] 10.5 μ m, [Ne III] 15.53 μ m and [Ne V] 14.3 μ m.

All studied SB galaxies show PAH bands and the following forbidden emission lines: [Si II] 34.8 μ m, [Ar II] 6.9 μ m, [S III] 18.7 and 33.4 μ m. In addition, nearly 80% show molecular H₂ lines. Similarly, \geq 80% of the Sy 2 show PAH features, and the same ionic lines detected in SB galaxies. However, we have found that PAH lines in Sy 1 galaxies behave differently from the other types of nuclear activity. The PAH bands at 7.7 μ m, 11.3 μ m and 12.7 μ m are present in 80% of the galaxies, but only 50% of them show the PAH lines at 6.2 μ m and 8.6 μ m. Nevertheless, the high ionization lines, such as [Ne V] 14.3 μ m and [O IV] 25.8 μ m are more common in Sy 1.

3.3. Diagnostic Diagram of PAH bands: grain sizes and ionization fraction

Numerical studies of the vibrational energy distribution of PAH molecules show that the relative strengths of the 3.3 μ m, 6.2 μ m, 7.7 μ m, 8.6 μ m and 11.3 μ m PAH features depend on grain size and on the charging conditions (Draine & Li 2001). Small PAHs radiate strongly at 6.2 μ m and 7.7 μ m, while large PAHs emit mostly at longer wavelengths (Schutte et al. 1993; Draine & Li 2007; Tielens 2008). Another important conclusion of Draine & Li (2001) is that neutral PAHs have higher values of 11.3 μ m/7.7 μ m ratio, while ionized PAHs have lower ratios. On the other hand, the 6.2 μ m/7.7 μ m ratio decreases with the increasing number of carbon atoms of the PAH molecules, Fig. 16 from Draine & Li (2001) shows how the relative strengths of these emission vary de-

pending on the size and charge state of PAH molecules. O'Dowd et al. (2009) used this diagram to analyze these PAH ratios for a sample formed by galaxies dominated by star formation, galaxies with significant stellar and AGN component and AGN-dominated galaxies. They found a weak trend in the direction of constant ionization fraction with changing grain size. In addition, they suggest that the presence of an AGN component is correlated with the reduction in the 7.7 μ m/11.3 μ m ratio indicating that smaller PAH grains (number of carbon atoms <180) are destroyed in AGNs.

We present in Fig. 5 the theoretical intensity ratios, for neutral and ionized PAHs (6.2 μ m/7.7 μ m \times 11.3 μ m/7.7 μ m), from Draine & Li (2001). The authors calculated these quantities assuming grains illuminated either by the Mathis et al. (1983) spectrum or a blackbody with T= 3 \times 10⁴K varying the number of carbon atoms in each molecule. We overplot in this diagram the observed PAH emission line ratios of our sample. Clearly, the observed ratios are located between neutral and ionized PAH theoretical lines, in agreement with previous studies (Draine & Li 2001; O'Dowd et al. 2009).

The above results suggest that the observed PAH bands in both, AGNs and low ionization objects (SB and LINERS), are formed by an appropriate mixture of PAH molecules with different sizes and adequate neutral to ionized fraction. High ionization objects (AGNs) present a tendency for molecules > 180 carbon atoms (6.2 μ m/7.7 μ m < 0.2), on the other hand most of low ionization objects are biased towards molecules with less than 180 carbon atoms. The latter are typically located in the region 0.2 < 6.2 μ m/7.7 μ m < 0.4 (Fig. 5). Furthermore, Seyfert galaxies appear to be located near to region populated by ionized PAH molecules, while the majority of SB, HII, and LINER are near to the line representing the neutral PAHs. Moreover, these results are consistent with a picture that AGN have higher ionization fraction and larger PAH molecules than SB galaxies.

Another way to assess the ionization fraction of the PAH molecules is using the following diagnostic diagram 6.2 μ m/11.3 μ m \times 7.7 μ m/11.3 μ m. Such diagram was used by Galliano (2006), Galliano et al. (2008) and O'Dowd et al. (2009),

they demonstrate that there is a good correlation between both ratios. However, we would like to emphasize the fact that both samples were mostly composed by SB galaxies. In addition, these ratios are controlled by the fraction of ionized to neutral PAHs (Allamandola et al. 1999).

In Fig 6 (top) we show these diagram for our sample. Clearly, if we only consider the SB galaxies our results are consistent with the correlation described above. By including the AGNs (Sy 1 and Sy 2), an unexpected large dispersion is observed for both type of activity. Alternatively, we also test the diagram $6.2\mu\text{m}/8.6\mu\text{m} \times 7.7\mu\text{m}/8.6\mu\text{m}$ involving ionized ($7.7\mu\text{m}$ and $6.2\mu\text{m}$) and neutral ($8.6\mu\text{m}$) PAH molecules. This diagram is shown in Fig.6 (bottom), where a similar dispersion is observed. Interestingly, in both diagnostic diagrams the ratios in the vertical axes tend to separate the AGNs (Sy 1 and Sy 2) from SB galaxies. This is even clearer in the diagram involving the $7.7\mu\text{m}/8.6\mu\text{m}$ ratio, leading us to the conclusion that $7.7\mu\text{m}/8.6\mu\text{m} \geq 6$ for AGNs (dotted line) and smaller for low ionization objects.

Synthetic spectra in the $6.2\mu\text{m} - 9.0\mu\text{m}$ region, for large symmetric PAHs cations, anions and neutral, have been computed by Bauschlicher et al. (2008). The trends, in the band position and intensity, is a function of the molecule size, charge and geometry. Large PAH cations and anions (> 110 carbon atoms) produce prominent bands at $7.7\mu\text{m}$ and $8.5\mu\text{m}$, the intensity ratio $7.7\mu\text{m}/8.6\mu\text{m}$ increase with the PAH sizes. Thus, we interpret the separation in activity types (SB, Sy 1 and Sy 2), along the vertical axis in both diagrams of Fig. 6, as due to the fact that in average the emitting PAH molecules in Seyferts are larger than those of SB. In addition, we suggest that the high values for the ratios $7.7\mu\text{m}/8.6\mu\text{m}$ and $7.7\mu\text{m}/11.3\mu\text{m}$ is due to the fact that almost all the molecules are ionized. In summary, we point out that both diagrams (Figs. 5 and 6) clearly shows that the ionization fraction and molecules size increase from SB to AGNs. However, it is worth mentioning that, no separation between Seyfert type is observed.

Although, the four ratios depends on the PAHs ionization fractions, ratios involving $6.2\mu\text{m}$ band have the same range of variation for both types of nuclear activity. This can be associated with

the fact that the $6.2\mu\text{m}$ PAH emission is due to small molecules (Bauschlicher et al. 2008), which probably are destroyed by the hard radiation field of Seyfert galaxies.

3.4. Diagnostic Diagram for Emission Line Objects

As shown in Sect. 3.2 (Fig. 3), forbidden ionic emission lines are observed in SB and active galaxies. In the first case, the gas is ionized by massive hot stars, while in the latter the ionization is due to a non-thermal continuum. Moreover, the emission cloud in AGNs are located in the narrow line regions (NLR) (Osterbrock & Ferland 2006).

The Mid-IR emission from dusty NLR of AGNs has been explored by Groves et al. (2006). Their models give a direct connection between the dust emission and the line emission from the photoionized gas. These authors also show that the emission line ratios $[\text{Ne V}]/[\text{Ne II}] \times [\text{Ne III}]/[\text{Ne II}]$ can be used to separate AGNs from SBs. In addition, Thornley et al. (2000) using starburst evolutionary models, which incorporate new stellar atmosphere models for massive stars, found that $[\text{Ne III}]/[\text{Ne II}]$ is sensitive to hardness of the radiation field.

In Fig. 7 we show the diagnostic diagram $[\text{Ne V}]14.3\mu\text{m}/[\text{Ne II}]12.8\mu\text{m} \times [\text{Ne III}]15.5\mu\text{m}/[\text{Ne II}]12.8\mu\text{m}$ for our sample. We also overplot the NLR models for different ionization and pressure parameters taken from Groves et al. (2006). Clearly, all the observations have values lower than those predicted by the models. In this diagram, AGNs are closely correlated, while the SB galaxies show a large scattering.

The $[\text{Ne V}]14.3\mu\text{m}$ has a high ionization potential of 97.1 eV and is often detected in spectra of AGNs (e.g. Sturm et al. 2002; Weedman et al. 2005) however is rarely detected in SB galaxies (Brandl et al. 2006; Bernard-Salas et al. 2009). The lack of correlation for SB galaxies in this diagram, thus, may be due to a strong contamination of $[\text{Ne V}]$ with PAH $14.19\mu\text{m}$ emission or to the absence of the former line in the SB galaxies spectra. In addition, we call the attention to the fact that the deblending of these lines is very difficult in the low resolution Spitzer spectra.

It is also clear in this figure that Sy 1 galaxies have $[\text{Ne III}]/[\text{Ne II}] \geq 0$, while SB and Sy 2

have this ratio ≤ 0 (solid line in Fig. 7). This suggests that both line ratios are sensitive to the hardness of the radiation field, confirming the result of Thornley et al. (2000). The fact that Sy 2 galaxies are spread over the lower left of the Fig. 7 can be associated to Groves et al. (2006) predictions, which states that starburst contribution would move the points in that direction.

It is worth mentioning that there are 3 SB galaxies located in the top-right side of Fig. 7 (NGC1097, NGC4676 and NGC520). The former, was reclassified as Sy 1 by Storchi-Bergmann et al. (1997), while the two latter are strongly interacting sources and may have the these emission lines enhanced (Read & Ponman 1998). Thus we suggest that further, more accurate studies (i.e. with higher spectral resolution spectra), are necessary to better explain the position of the SB galaxies in the diagram.

4. Behavior of the Ionization Fraction and EW of PAH Molecules with the Hardness of Radiation Field

Smith et al. (2007) have studied the correlation between the intensity ratio of the strongest PAH bands $7.7\mu\text{m}/11.3\mu\text{m}$ with the hardness of the radiation field indicator, $[\text{Ne III}]/[\text{Ne II}]$. They have found that galaxies with HII regions or starburst optical spectra exhibit a nearly constant $7.7\mu\text{m}/11.3\mu\text{m}$ across the whole range of radiation hardness, including low-metallicity galaxies, which have $[\text{Ne III}]/[\text{Ne II}] < 2$. In contrast, the AGNs are located below the HII-type galaxies and their PAH ratio falls rapidly with increasing radiation field. This result was confirmed by O'Dowd et al. (2009) through the analysis of PAH emission bands of a sample of 92 typical star forming galaxies. They interpreted the decrease in the PAHs band ratio for AGNs as due to a selective destruction of the ionized $7.7\mu\text{m}$ PAH molecules.

The variation of $7.7\mu\text{m}/11.3\mu\text{m}$ PAH bands, observed in our sample (186 objects), with respect to the hardness of the radiation field, is shown in Fig. 8. It is clear from this figure, that the fraction of ionized to neutral PAH bands does not depend on the hardness of the radiation field in contrast with the previous results of Smith et al. (2007) and O'Dowd et al. (2009). We interpret this behavior as due to the fact that the strengths of both

PAH bands would have the same dependence on the radiation field.

Besides, this diagram show a tendency in the sense that SB galaxies have $[\text{Ne III}]/[\text{Ne II}] < 0.4$, while for Sy 1 and Sy 2 $[\text{Ne III}]/[\text{Ne II}] > 0.4$. In addition, Sy 1 are biased towards location on the upper right corner. Some of the Sy 2 galaxies are located in the SB region, which suggest that these galaxies may have a circumnuclear starburst. No clear separation between Sy 1 and Sy 2 is observed for $[\text{Ne III}]/[\text{Ne II}] > 0.4$.

In order to test the dependence of the PAH bands strength with the radiation field, we compare in Fig. 9 the EW of the $7.7\mu\text{m}$ and $11.3\mu\text{m}$ PAH bands with $[\text{Ne III}]/[\text{Ne II}]$ hardness indicator. It can be seen that EW of both PAH bands are constant with the radiation field indicator for $[\text{Ne III}]/[\text{Ne II}] \leq 0.8$, and fall rapidly with the increasing radiation field. Galaxies, powered by star formation, have a nearly constant EW across the full range of $[\text{Ne III}]/[\text{Ne II}]$. While for Sy 1 the EWs of the PAH bands decrease rapidly, for the Sy 2 the EW values are distributed either in the SB or Sy 1 region. Their location in the diagram may reflect the stellar or AGNs dominant component contribution to the spectra (i.e. in some case the Sy 2 may be dominated by a non-thermal component, and in other by circumnuclear massive star formation). In order to have a more quantitative analysis of Fig. 9, we have computed an exponential regression taking into account all objects (AGNs+SBs, dotted line) and another for a subsample formed only by AGNs (solid line). For the latter we have found a correlation coefficient of ~ -0.7 while for the former we have not found any correlation (~ -0.2).

We conclude this section by arguing that both PAH molecules, either ionized ($7.7\mu\text{m}$) or neutral ($11.3\mu\text{m}$), may be destroyed with increasing hardness of the radiation field. We emphasize that similar results were found by Genzel et al. (1998), which compares the PAH strength with the high to low excitation line ratios for a sample of ULIRS (ultra luminous infrared galaxies) and AGNs. In addition, Baum et al. (2010) has shown that the diagram EW PAH $6.2\mu\text{m} \times [\text{Ne V}] 14.3\mu\text{m}/[\text{Ne II}] 12.8\mu\text{m}$ separate AGNs from SB galaxies.

5. Summary and Conclusions

We have analyzed the emission line properties of a sample of 186 Spitzer galaxy spectra. 171 objects were taken from the literature and we have added 15 unpublished AGNs Spitzer spectra, taken from the public archive. The continuum properties of the 15 new spectra were also studied. Our main results can be summarized as follows.

- The normalized Mid-IR continuum spectra (at $\lambda = 23\mu\text{m}$), of the 15 new AGNs, steeply rise for redder wavelengths and can be fitted with a warm blackbody distribution of $T \sim 150\text{-}300\text{ K}$.
- The brightest PAH spectral bands ($6.2, 7.7, 8.6, 11.3,$ and $12.7\mu\text{m}$) and the forbidden emission lines of $[\text{Si II}] 34.8\mu\text{m}$, $[\text{Ar II}] 6.9\mu\text{m}$, $[\text{S III}] 18.7$ and $33.4\mu\text{m}$ were detected in all the SB and in $\sim 80\%$ of the Sy 2. Taking under consideration only the PAH bands at $7.7\mu\text{m}$, $11.3\mu\text{m}$, and $12.7\mu\text{m}$ we find they are present in $\sim 80\%$ of the Seyfert 1, while only half of this type of activity show the $6.2\mu\text{m}$ and $8.6\mu\text{m}$ PAH bands.
- Comparison between observed line intensity ratios of neutral and ionized PAHs ($6.2\mu\text{m}/7.7\mu\text{m} \times 11.3\mu\text{m}/7.7\mu\text{m}$) with theoretical models suggests that these ratios, in Sy 1, Sy2 and SB galaxies, are produced by an appropriate mixture of PAH molecules, with different sizes and adequate neutral to ionized fraction.
- The PAH emission lines observed in Sy 1 and Sy 2 may be due to PAH molecules with > 180 carbon atoms, while for most of the low ionization objects (SB and LINERs) it is biased towards molecules with < 180 carbon atoms. In addition, Seyfert galaxies appear to be located near to region populated by ionized PAH molecules, while the majority of SB, HII, and LINER populate the region of neutral PAHs. These results are consistent with a picture where Sy 1 and Sy 2 have higher ionization fraction and larger PAH molecules than SB galaxies.
- We have investigated the PAH line intensity ratio diagrams $6.2\mu\text{m}/11.3\mu\text{m} \times 7.7\mu\text{m}/$

$11.3\mu\text{m}$ and $6.2\mu\text{m}/8.6\mu\text{m} \times 7.7\mu\text{m}/8.6\mu\text{m}$. The separation in activity types (SB, Sy 1 and Sy2), along the vertical axis in both diagrams, is interpreted as due to the fact that in average the emitting PAH molecules in Seyferts are larger than those of SB, with ionization fraction and emitting molecules sizes increasing from SB to AGNs. No separation between Seyfert type is observed.

- Diagnostic diagram $[\text{Ne V}]14.3\mu\text{m}/[\text{Ne II}]12.8\mu\text{m} \times [\text{Ne III}]15.5\mu\text{m}/[\text{Ne II}]12.8\mu\text{m}$ shows that AGNs are correlated, while SB galaxies show a large scattering. Moreover, for most of the Sy 1 $[\text{Ne III}]/[\text{Ne II}] \geq 0$, while for SB and Sy 2s $[\text{Ne III}]/[\text{Ne II}] \leq 0$, indicating that both line ratios can be used as an indicator of radiation field hardness.
- The ratio between the $7.7\mu\text{m}$ and $11.3\mu\text{m}$ PAH bands is nearly constant with the increase of $[\text{Ne III}]15.5\mu\text{m}/[\text{Ne II}]12.8\mu\text{m}$, indicating that the fraction of ionized to neutral PAH bands does not depend on the hardness of the radiation field.
- The equivalent width of both PAH features ($7.7\mu\text{m}$ and $11.3\mu\text{m}$) show the same dependence with the $[\text{Ne III}]/[\text{Ne II}]$ ratio. In the case of Sy 1, they are nearly constant for $[\text{Ne III}]/[\text{Ne II}] \leq 0.8$, and fall sharply with increasing radiation field. For SB galaxies the PAH EW is constant with the increase of $[\text{Ne III}]/[\text{Ne II}]$. Sy 2s are distributed either in the SB or Sy 1 regions. These results suggest that the PAH molecules emitting either ionized ($7.7\mu\text{m}$) or neutral ($11.3\mu\text{m}$) bands, may be destroyed with increasing hardness of the radiation field.

We thank an anonymous referee for useful comments, as well as Charles Bonatto, Daniel Ruschel-Dutra and Rogemar André Riffel for useful discussions. This research has made use of the NASA/IPAC Extragalactic Database (NED) which is operated by the Jet Propulsion Laboratory, California Institute of Technology, under contract with the National Aeronautics and Space Administration. This work is based on observations made with the Spitzer Space Telescope,

which is operated by the Jet Propulsion Laboratory, California Institute of Technology under a contract with NASA.

REFERENCES

- Allamandola, L. J., Hudgins, D. M., & Sandford, S. A. 1999, *ApJ*, 511, L155
- Baum, S. A., Gallimore, J. F., O’Dea, C. P., Buchanan, C. L., Noel-Storr, J., Axon, D. J., Robinson, A., Elitzur, M., Dorn, M., & Staudaher, S. 2010, *ApJ*, 710, 289
- Bauschlicher, Jr., C. W., Peeters, E., & Allamandola, L. J. 2008, *ApJ*, 678, 316
- Brandl, B. R., Bernard-Salas, J., Spoon, H. W. W., Devost, D., Sloan, G. C., Guilles, S., Wu, Y., Houck, J. R., Weedman, D. W., Armus, L., Appleton, P. N., Soifer, B. T., Charmandaris, V., Hao, L., Higdon, J. A., Marshall, S. J., Herter, T. L. 2006, *ApJ*, 653, 1129
- Buchanan, C. L., Gallimore, J. F., O’Dea, C. P., Baum, S. A., Axon, D. J., Robinson, A., Elitzur, M., & Elvis, M. 2006, *AJ*, 132, 401
- Bernard-Salas, J., Spoon, H. W. W., Charmandaris, V., Leboutellier, V., Farrah, D., Devost, D., Brandl, B. R., Wu, Y., Armus, L., Hao, L., Sloan, G. C., Weedman, D., & Houck, J. R. 2009, *ApJS*, 184, 230
- Burtscher, L., Jaffe, W., Raban, D., Meisenheimer, K., Tristram, K. R. W., & Röttgering, H. 2009, *ApJ*, 705, L53
- Deo, R. P., Richards, G. T., Crenshaw, D. M., & Kraemer, S. B. 2009, *ApJ*, 705, 14
- Draine, B. T., & Lee, H. M. 1984, *ApJ*, 285, 89
- Draine, B. T., & Li, A. 2001, *ApJ*, 551, 807
- Draine, B. T., & Li, Aigen 2007, *ApJ*, 657, 810
- Galliano, F. 2006, arXiv:astro-ph/0610852
- Galliano, F., Madden, S. C., Tielens, A. G. G. M., Peeters, E., Jones, A. P. 2008, 679, 310
- Gallimore, J. F., Yzaguirre, A., Jakoboski, J., Stevenosky, M. J., Axon, D. J., Baum, S. A., Buchanan, C. L., Elitzur, M., Elvis, M., O’Dea, C. P., & Robinson, A. 2010, *ApJ*, 187, 172
- Genzel, R., et al. 1998, *ApJ*, 498, 579
- Gordon, K. D., Engelbracht, C. W., Rieke, G. H., Misselt, K. A., Smith, J.-D. T., & Kennicutt, R. C., Jr. 2008, *ApJ*, 682, 336
- Groves, B., Dopita, M., & Sutherland, R. 2006, *A&A*, 458, 405
- Houck, J. R., et al. 2004, *ApJS*, 154, 18
- Hunt, L. K., Thuan, T. X., Izotov, Y. I., & Sauvage, M. 2010, *ApJ*, 712, 164
- Kaneda, H., Onaka, T., Sakon, I., Kitayama, T., Okada, Y., & Suzuki, T. 2008, 684, 270
- Mathis, J. S., Mezger, P. G., & Panagia, N. 1983, *A&A*, 128, 212
- O’Dowd, M. J., Schiminovich, D., Johnson, B. D., Treyer, M. A., Martin, C. D., Wyder, T. K., Charlot, S., Heckman, T. M., Martins, L. P., Seibert, M., & van der Hulst J. M. 2009, *ApJ*, 705, 885
- Osterbrock, Donald E. & Gary J. Ferland, *Astrophysics of Gaseous Nebulae and Active Galactic Nuclei*, 2nd Ed. (University Science Books, Sausalito, CA, 2006)
- Pogge, R. W., & Owen, J. M. 1993, OSU Internal Report 93-01
- Puget, J. L., & Leger, A. 1989, *ARA&A*, 27, 161
- Read, A. M., & Ponman, T. J. 1998, *MNRAS*, 297, 143
- Riffel, R., Rodríguez-Ardila, A., & Pastoriza, M. G. 2006, *A&A*, 457, 61
- Riffel, R., Pastoriza, M. G., Rodríguez-Ardila, A., & Bonatto, C. 2009, *MNRAS*, 400, 273
- Roche, P. F., Aitken, D. K., Smith, C. H., & Ward, M. J. 1991, *MNRAS*, 248, 606
- Schutte, W. A., Tielens, A. G. G. M., & Allamandola, L. J., 1993, *ApJ*, 415, 397
- Smith, J. D. T., Draine B. T., Dale D. A., et al. 2007, *ApJ*, 656, 770
- Storchi-Bergmann, T., Eracleous, M., Ruiz, M. T., Livio, M., Wilson, A. S., & Filippenko, A. V. 1997, *ApJ*, 489, 87

Sturm, E., Lutz, D., Tran, D., Feuchtgruber, H., Genzel, R., Kunze, D., Moorwood, A. F. M., & Thornley, M. D. 2000, *A&A*, 358, 481

Sturm, E., Lutz, D., Verma, A., Netzer, H., Sternberg, A., Moorwood, A. F. M., Oliva, E., & Genzel, R. 2002, *A&A*, 393, 821

Thornley, M. D., Schreiber, N. M. F., Lutz, D., Genzel, R., Spoon, H. W. W., Kunze, D., & Sternberg, A. 2000, *ApJ*, 539, 641

Tielens, A. G. G. M. 2008, *ARA&A*, 46, 289

Voit, G. M. 1992, *ApJ*, 399, 495a

Voit, G. M. 1992, *MNRAS*, 258, 841b

Weedman, D. W., et al. 2005, *ApJ*, 633, 706

Wu, Y., Charmandaris, V., Huang, J., Spinoglio, L., Tommasin, S. 2009, *ApJ*, 701, 658

Table 1: Sample properties

Name	RA ¹	DEC ¹	z ¹
Sey 1			
Mrk279	13h53m03.4s	+69d18m30s	0.030451
Mrk334	00h03m09.6s	+21d57m37s	0.021945
Mrk478	14h42m07.4s	+35d26m23s	0.079055
NGC4748	12h52m12.4s	-13d24m53s	0.014630
Sey 2			
Mrk3	06h15m36.3s	+71d02m15s	0.013509
Mrk471	14h22m55.4s	+32d51m03s	0.034234
Mrk609	03h25m25.3s	-06d08m38s	0.034488
Mrk622	08h07m41.0s	+39d00m15s	0.023229
Mrk883	16h29m52.9s	+24d26m38s	0.037496
Mrk1066	02h59m58.6s	+36d49m14s	0.012025
NGC1275	03h19m48.1s	+41d30m42s	0.017559
NGC2622	08h38m10.9s	+24d53m43s	0.028624
NGC3786	11h39m42.5s	+31d54m33s	0.008933
NGC5728	14h42m23.9s	-17d15m11s	0.009353
NGC7682	23h29m03.9s	+03d32m00s	0.017140

¹Taken from the NASA Extra-galactic Database (NED).

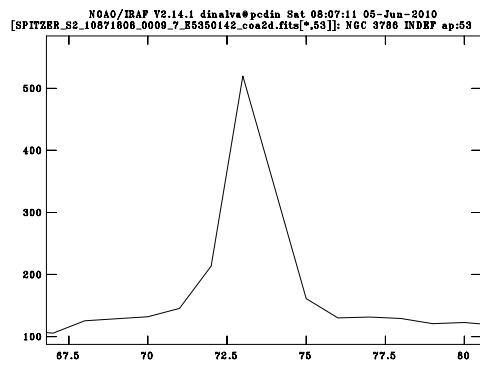
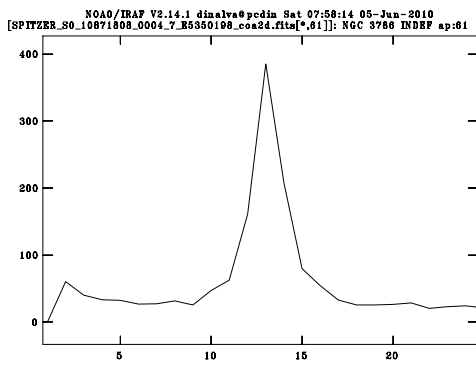


Fig. 1.— Spatial emission profile of NGC3786 for the SL (left) and LL (right) modules.

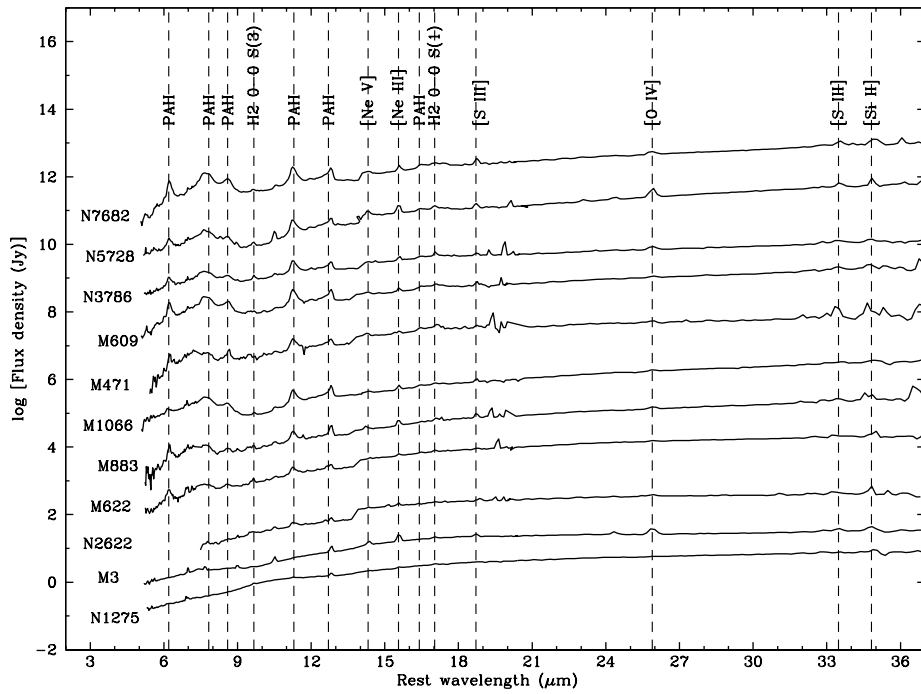
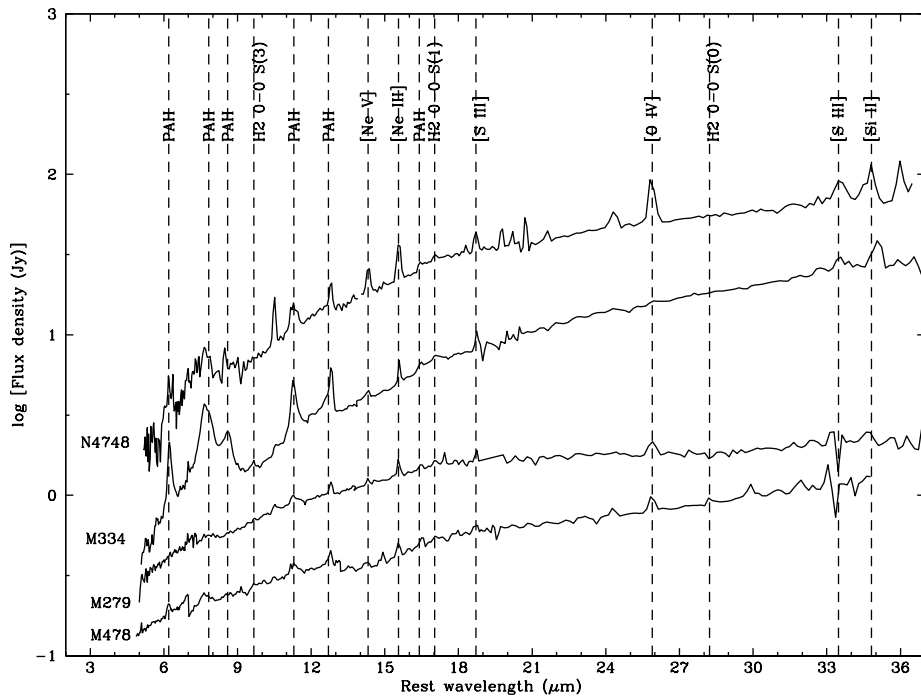


Fig. 2.— Calibrated spectra of the Sy 1 (top) and Sy 2 (bottom) galaxies. All spectra were ordered according to their shapes from a steeper spectrum (top) to a flatter one (bottom). Some emission lines are identified. All spectra were normalized at $23\mu\text{m}$.

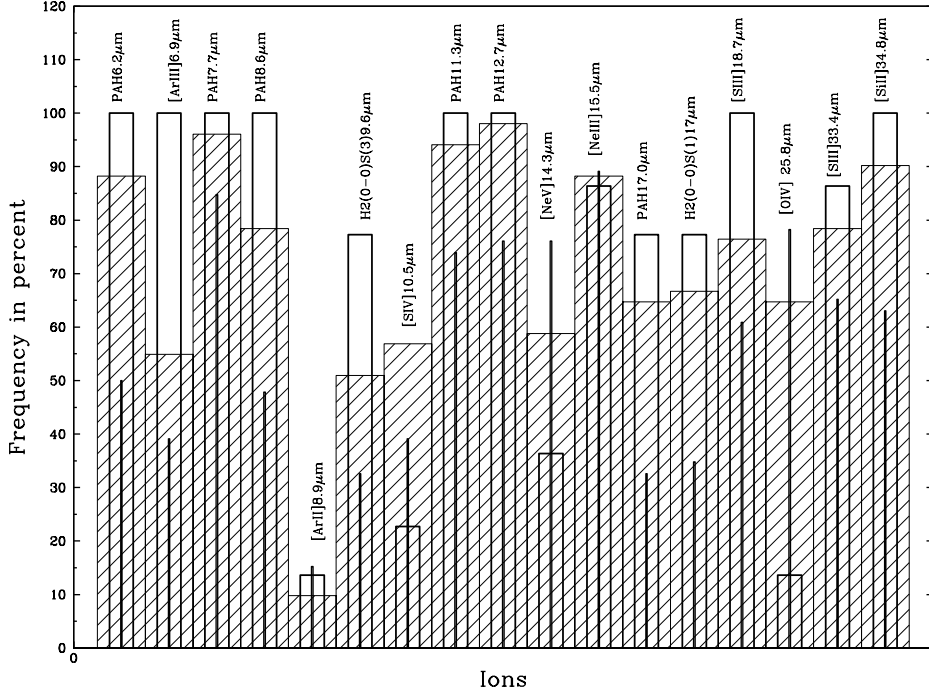


Fig. 3.— Frequency histogram of most common Mid-IR emission lines (in percent). SB, Sy 2 and Sy 1 are represented by empty and shaded bars, and solid lines, respectively.

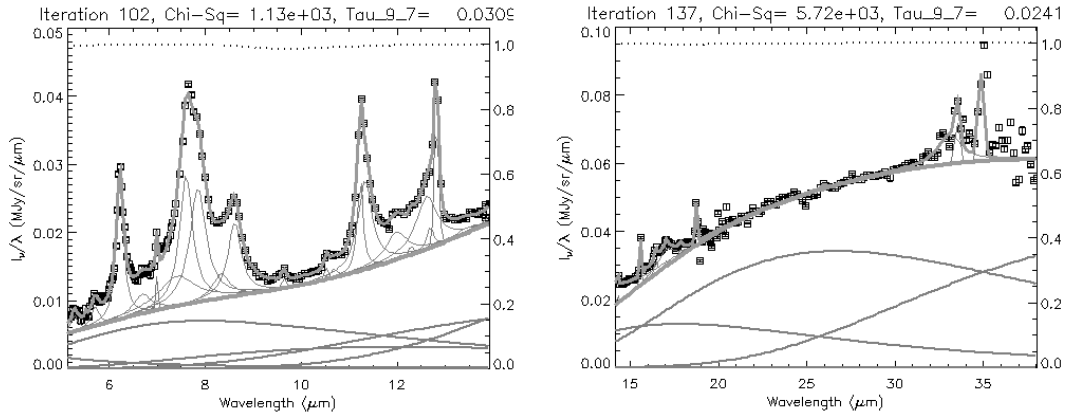


Fig. 4.— Detailed decomposition of Mrk334 from 5 to $37\mu\text{m}$ using PAHFIT code. Solid black lines represent thermal dust continuum components. Measurements are represented by squares, uncertainties are plotted as vertical error-bars, which are smaller than the symbol size. Dotted black line indicates mixed extinction components. Continuous lines (gray) represent the best fit model with individual PAH features and emission lines, respectively.

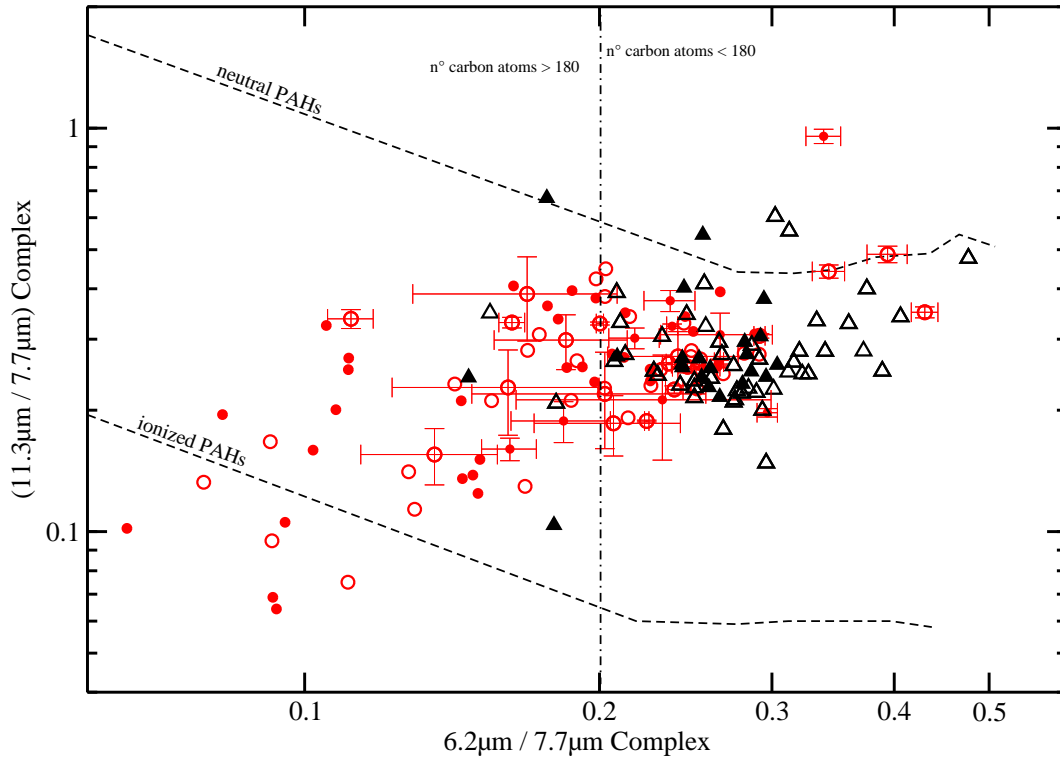


Fig. 5.— Diagnostic diagram of $6.2\mu\text{m}/7.7\mu\text{m} \times 11.3\mu\text{m}/7.7\mu\text{m}$ PAH ratios. The long dash line represents theoretical intensities of neutral to ionized PAHs (Draine & Li 2001). Dashed-dotted line shows the position of molecules formed by 180 carbon atoms. Empty triangles are HII and LINER objects taken from Smith et al. (2007) and Gordon et al. (2008), full triangles are SB taken from Brandl et al. (2006), full and empty circles are Sy 1 and Sy 2 of our and Gallimore et al. (2010) sample. Error bars are shown only for the 15 new AGNs, similar error were found for the remaining objects.

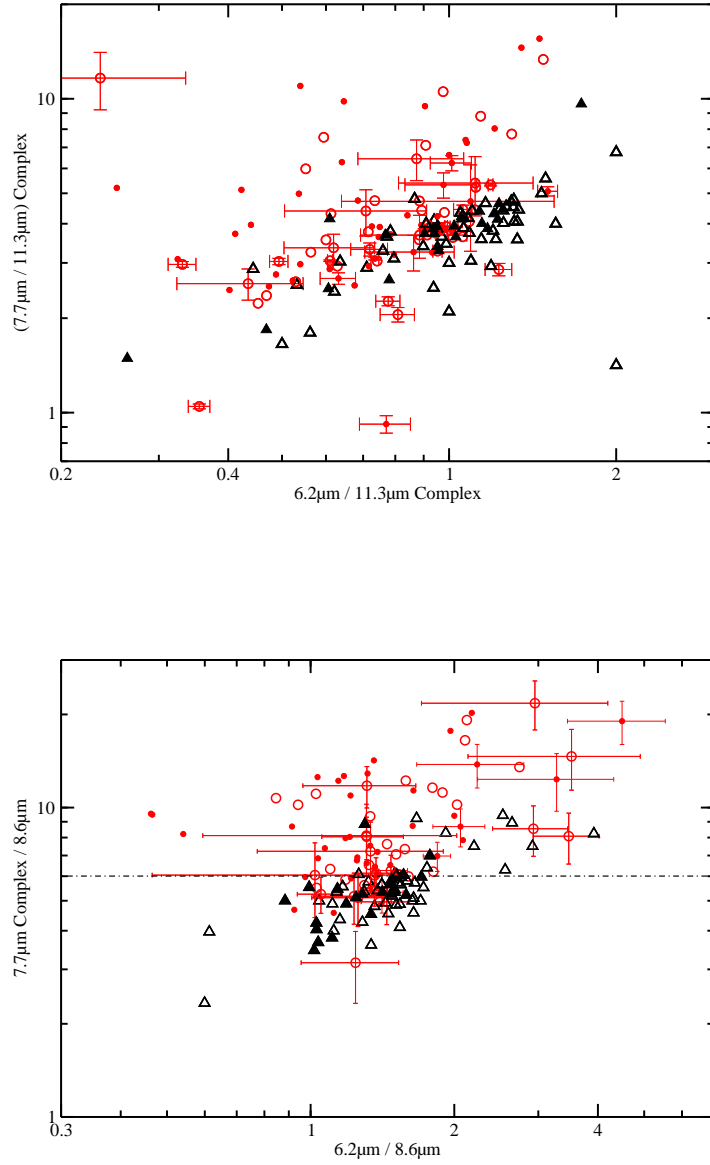


Fig. 6.— Diagnostic diagram of the relative strengths of the neutral ($8.6\ \mu\text{m}$ and $11.3\ \mu\text{m}$) compared to ionized ($6.2\ \mu\text{m}$ and $7.7\ \mu\text{m}$) PAH bands. In the top, $6.2\ \mu\text{m}/11.3\ \mu\text{m} \times 7.7\ \mu\text{m}/11.3\ \mu\text{m}$ PAHs. Empty triangles are HII and LINER objects taken from Smith et al. (2007) and Gordon et al. (2008), full triangles are SB taken from Brandl et al. (2006), full and empty circles are Sy 1 and Sy 2 of our and Gallimore et al. (2010) sample. Error bars are shown only for the 15 new AGNs, similar error were found for the remaining objects. Dotted line separate high and low ionization objects.

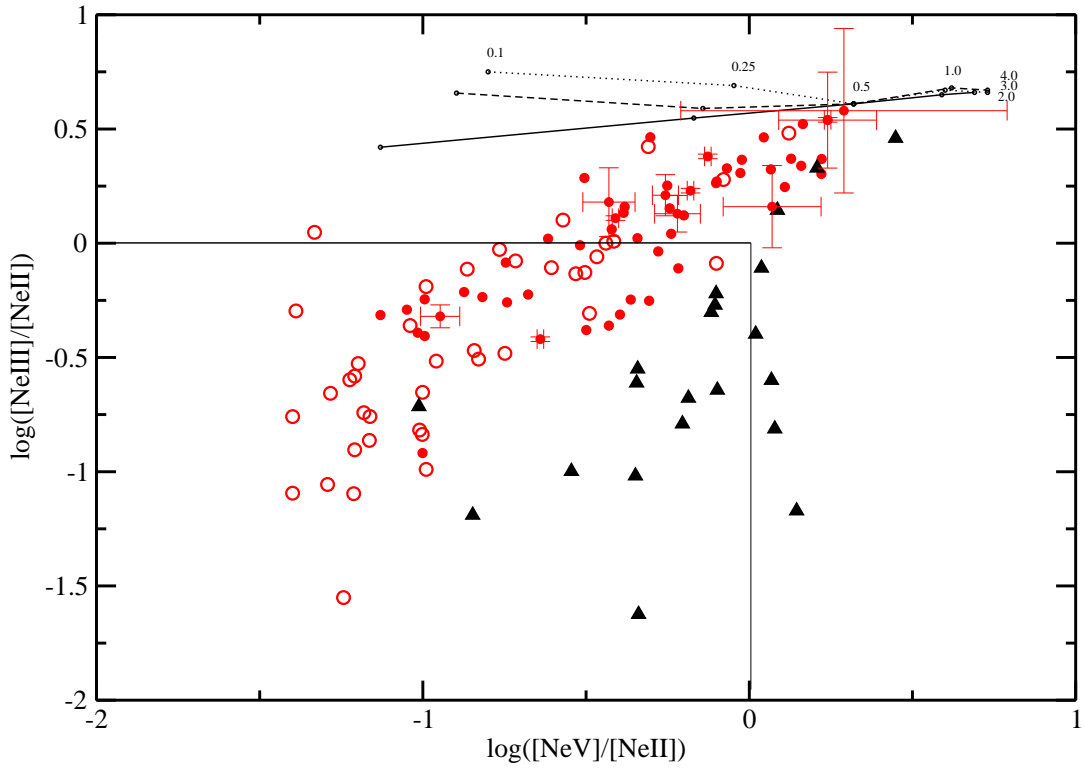


Fig. 7.— Diagnostic diagram of $[\text{Ne V}] 14.3\mu\text{m}/[\text{Ne II}] 12.8\mu\text{m} \times [\text{Ne III}] 15.5\mu\text{m}/[\text{Ne II}] 12.8\mu\text{m}$ ratios. The direction of increasing ionization parameter for dusty NLR models with the total pressure of: $P_{tot}/k \simeq 10^6$ (dot curve), $\simeq 10^7$ (dashed curve) and $\simeq 10^8$ (solid curve). Full triangles are SB taken from Brandl et al. (2006), full and empty circles are Sy 1 and Sy 2 of our and Gallimore et al. (2010) sample. Error bars are shown only for the 15 new AGNs, similar error were found for the remaining objects.

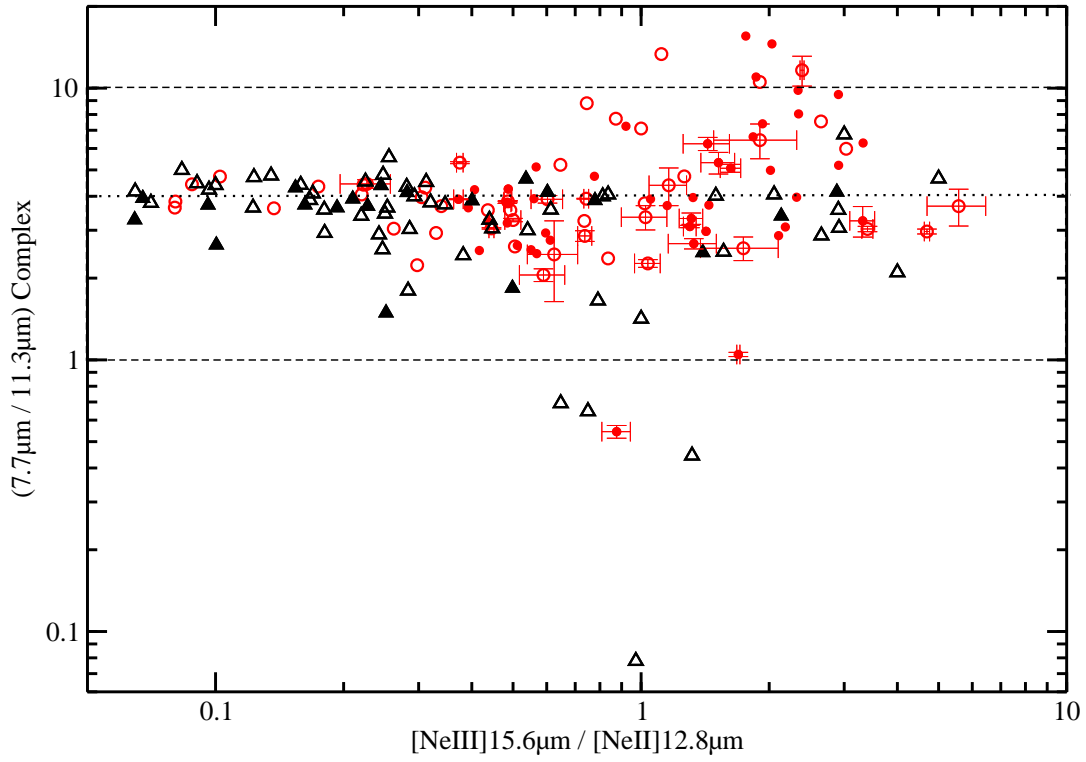


Fig. 8.— Diagnostic diagram between an indicator of the hardness of the radiation field, $[\text{Ne III}] 15.5 / [\text{Ne II}] 12.8 \mu\text{m} \times 7.7 \mu\text{m} / 11.3 \mu\text{m}$ PAH emission features. Empty triangles are HII and LINER objects taken from Smith et al. (2007) and Gordon et al. (2008), full triangles are SB taken from Brandl et al. (2006), full and empty circles are Sy 1 and Sy 2 of our and Gallimore et al. (2010) sample. Error bars are shown only for the 15 new AGNs, similar error were found for the remaining objects.

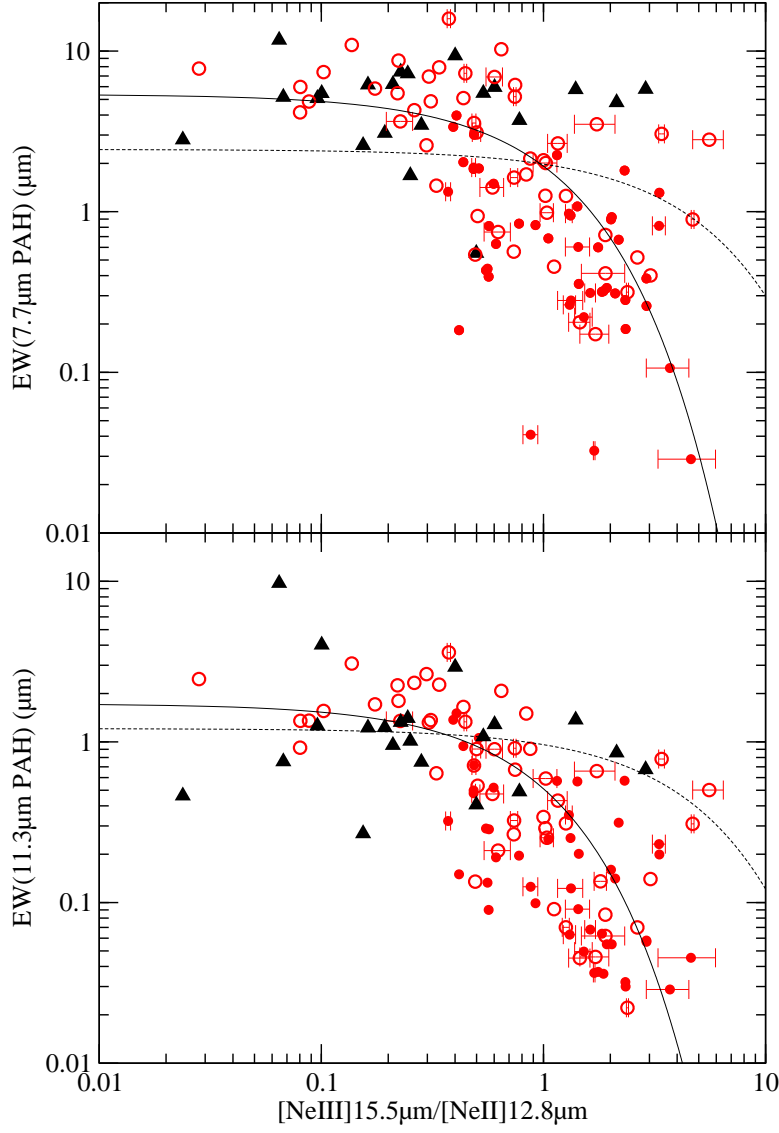


Fig. 9.— Diagnostic diagram between an indicator of the hardness of the radiation field, $[\text{Ne III}] 15.5 / [\text{Ne II}] 12.8 \mu\text{m}$ versus EW $7.7 \mu\text{m}$ (top) and EW $11.3 \mu\text{m}$ (bottom) PAH emission features. Full triangles are SB taken from Brandl et al. (2006), full and empty circles are Sy 1 and Sy 2 of our and Gallimore et al. (2010) sample. Error bars are shown only for the 15 new AGNs, similar error were found for the remaining objects. The lines represent an exponential regression fitted for the total sample (dotted line) and for AGNs sub-sample (solid line).

Table 2: Aromatic Emission Line Strengths ($10^{-16} W m^{-2}$) and Equivalent Widths (μm).

Name	6.2 μm	Ew	6.7 μm	Ew	7.7 μm	Ew	8.3 μm	Ew	8.6 μm	Ew	10.7 μm	Ew	11.3 μm	Ew	12.0 μm	Ew	12.7 μm	Ew	17.0 μm	Ew
Sy 1																				
Mrk279	2.88 \pm 0.33	0.035	7.19 \pm 0.81	0.095	15.6 \pm 1.82	0.220	-	-	0.09 \pm 0.26	0.001	0.84 \pm 0.12	0.013	2.94 \pm 0.36	0.049	-	-	0.15 \pm 0.10	0.002	6.62 \pm 0.89	0.154
Mrk334	28.5 \pm 0.30	0.548	9.92 \pm 0.67	0.183	107 \pm 2.88	1.881	7.98 \pm 0.34	0.138	20.2 \pm 0.24	0.351	1.12 \pm 0.09	0.019	28.3 \pm 0.35	0.479	8.05 \pm 0.19	0.131	16.7 \pm 0.39	0.263	18.5 \pm 0.83	0.229
Sy 2																				
Mrk3	0.77 \pm 0.31	0.006	4.56 \pm 0.63	0.037	38.2 \pm 2.98	0.315	-	-	1.14 \pm 0.35	0.009	1.22 \pm 0.17	0.009	3.28 \pm 0.55	0.022	1.61 \pm 0.37	0.009	1.45 \pm 0.16	0.008	39.2 \pm 1.57	0.143
Mrk471	2.67 \pm 0.12	0.820	3.98 \pm 0.32	1.030	6.78 \pm 1.15	1.415	-	-	2.15 \pm 0.09	0.382	0.05 \pm 0.04	0.007	3.30 \pm 0.22	0.474	0.56 \pm 0.19	0.078	1.67 \pm 0.29	0.226	5.18 \pm 0.26	0.359
Mrk609	16.9 \pm 0.22	1.020	8.57 \pm 0.49	0.485	58.0 \pm 1.74	3.115	4.62 \pm 0.20	0.245	11.7 \pm 0.16	0.617	0.53 \pm 0.07	0.027	17.7 \pm 0.32	0.903	5.76 \pm 0.23	0.282	10.4 \pm 0.48	0.474	16.5 \pm 0.66	0.469
Mrk622	5.01 \pm 0.19	0.516	2.26 \pm 0.42	0.194	14.6 \pm 1.65	0.986	-	-	1.71 \pm 0.14	0.093	0.37 \pm 0.07	0.015	6.45 \pm 0.28	0.253	2.40 \pm 0.18	0.089	4.41 \pm 0.41	0.154	2.65 \pm 0.49	0.044
Mrk883	4.62 \pm 0.14	1.100	4.68 \pm 0.35	0.920	10.7 \pm 1.18	1.630	-	-	1.33 \pm 0.10	0.161	0.01 \pm 0.04	0.001	3.76 \pm 0.22	0.324	0.83 \pm 0.18	0.068	1.37 \pm 0.34	0.107	2.53 \pm 0.30	0.111
Mrk1066	47.0 \pm 0.28	0.757	15.5 \pm 0.58	0.263	199 \pm 2.76	3.567	18.6 \pm 0.37	0.340	31.9 \pm 0.26	0.592	1.29 \pm 0.11	0.020	52.1 \pm 0.43	0.713	15.3 \pm 0.23	0.181	30.9 \pm 0.45	0.328	43.0 \pm 1.41	0.325
NGC1275	10.8 \pm 0.25	0.097	18 \pm 0.48	0.139	-	-	-	-	10.6 \pm 0.10	0.043	17.4 \pm 0.33	0.070	2.90 \pm 0.22	0.011	-	-	-	-	53.9 \pm 0.98	0.199
NGC2622	2.75 \pm 0.14	0.233	4.33 \pm 0.37	0.339	-	-	-	-	0.32 \pm 0.05	0.015	2.97 \pm 0.21	0.135	0.78 \pm 0.14	0.034	2.03 \pm 0.13	0.086	2.42 \pm 0.46	0.0472	-	-
NGC5728	10.6 \pm 0.32	0.379	4.11 \pm 0.64	0.167	65.1 \pm 3.00	3.050	4.88 \pm 0.37	0.245	8.09 \pm 0.31	0.424	0.04 \pm 0.21	0.001	21.4 \pm 0.65	0.783	3.97 \pm 0.35	0.117	9.89 \pm 0.78	0.258	32.6 \pm 1.14	0.471
NGC7682	40.4 \pm 0.16	1.840	11.5 \pm 0.35	0.456	160 \pm 1.48	5.200	11.3 \pm 0.16	0.328	29.7 \pm 0.12	0.828	1.07 \pm 0.05	0.024	40.9 \pm 0.19	0.913	10.1 \pm 0.12	0.221	24.0 \pm 0.26	0.522	39.8 \pm 0.55	0.641

Table 3: Atomic Emission Line Strengths ($10^{-16} W m^{-2}$) and Equivalent Widths (μm).

Name	[Ar II]6.9 μm	Ew	[Ar III]8.9 μm	Ew	[S IV]10.5 μm	Ew	[Ne II]12.8 μm	Ew	[Ne III]15.5 μm	Ew	[S III]18.7 μm	Ew	[O IV]25.9 μm	Ew	[Fe II]25.9 μm	Ew	[S III]33.4 μm	Ew	[Si II]34.8 μm	Ew
Sy 1																				
Mrk279	0.70 \pm 0.16	0.014	0.05 \pm 0.10	0.001	0.60 \pm 0.05	0.014	0.82 \pm 0.05	0.022	1.26 \pm 0.07	0.039	0.64 \pm 0.10	0.024	1.10 \pm 0.05	0.067	-	-	-	-	0.87 \pm 0.13	0.088
Mrk334	1.36 \pm 0.09	0.036	0.06 \pm 0.05	0.001	0.63 \pm 0.03	0.016	5.32 \pm 0.03	0.122	2.58 \pm 0.04	0.050	2.91 \pm 0.06	0.050	-	-	0.49 \pm 0.06	0.008	3.82 \pm 0.14	0.068	7.07 \pm 0.14	0.129
Mrk478	0.47 \pm 0.03	0.012	0.06 \pm 0.06	0.002	0.38 \pm 0.04	0.016	0.59 \pm 0.04	0.032	0.52 \pm 0.01	0.032	0.40 \pm 0.01	0.027	0.75 \pm 0.02	0.066	-	-	-	-	0.01 \pm 0.06	0.001
NGC4748	0.45 \pm 0.21	0.030	0.28 \pm 0.12	0.018	2.34 \pm 0.09	0.144	1.14 \pm 0.06	0.065	3.78 \pm 0.12	0.123	1.83 \pm 0.15	0.058	6.81 \pm 0.13	0.269	-	-	2.69 \pm 0.24	0.131	3.42 \pm 0.29	0.167
Sy 2																				
Mrk3	3.31 \pm 0.19	0.040	2.63 \pm 0.12	0.034	6.26 \pm 0.08	0.072	8.75 \pm 0.08	0.073	20.9 \pm 0.12	0.111	6.70 \pm 0.11	0.037	18.2 \pm 0.10	0.159	-	-	4.25 \pm 0.20	0.054	11.7 \pm 0.20	0.156
Mrk471	0.43 \pm 0.06	0.153	-	-	0.12 \pm 0.01	0.028	0.32 \pm 0.02	0.064	0.19 \pm 0.01	0.020	0.13 \pm 0.02	0.013	0.36 \pm 0.02	0.049	-	-	1.74 \pm 0.03	0.285	2.03 \pm 0.08	0.331
Mrk609	1.02 \pm 0.08	0.083	-	-	0.29 \pm 0.02	0.022	2.22 \pm 0.03	0.144	1.11 \pm 0.04	0.047	1.19 \pm 0.05	0.048	0.82 \pm 0.03	0.034	-	-	1.59 \pm 0.08	0.070	3.63 \pm 0.13	0.159
Mrk622	0.40 \pm 0.08	0.046	-	-	0.34 \pm 0.02	0.021	0.70 \pm 0.03	0.036	0.73 \pm 0.03	0.019	0.39 \pm 0.07	0.009	0.73 \pm 0.04	0.020	-	-	0.80 \pm 0.09	0.028	3.51 \pm 0.14	0.128
Mrk883	0.55 \pm 0.06	0.147	0.11 \pm 0.02	0.019	0.26 \pm 0.02	0.036	1.31 \pm 0.02	0.150	0.96 \pm 0.03	0.069	0.71 \pm 0.03	0.043	0.91 \pm 0.02	0.058	-	-	0.82 \pm 0.05	0.052	2.58 \pm 0.09	0.161
Mrk1066	3.75 \pm 0.12	0.096	0.83 \pm 0.07	0.023	1.61 \pm 0.04	0.038	9.60 \pm 0.03	0.146	4.67 \pm 0.09	0.055	4.80 \pm 0.12	0.050	3.51 \pm 0.22	0.031	0.25 \pm 0.29	0.002	3.72 \pm 0.22	0.035	11.2 \pm 0.23	0.108
NGC1275	1.89 \pm 0.11	0.019	-	-	2.78 \pm 0.05	0.017	3.37 \pm 0.05	0.019	4.25 \pm 0.14	0.023	1.77 \pm 0.11	0.009	-	-	-	-	0.07 \pm 0.18	0.001	10.2 \pm 0.23	0.096
NGC3786	0.56 \pm 0.06	0.031	-	-	0.51 \pm 0.02	0.031	1.49 \pm 0.02	0.087	1.10 \pm 0.02	0.042	0.06 \pm 0.03	0.024	1.31 \pm 0.19	0.066	0.04 \pm 0.01	0.020	1.33 \pm 0.06	0.076	1.70 \pm 0.05	0.096
NGC2622	0.62 \pm 0.05	0.069	0.11 \pm 0.04	0.009	0.44 \pm 0.02	0.031	0.50 \pm 0.02	0.031	0.91 \pm 0.03	0.025	0.40 \pm 0.04	0.012	0.86 \pm 0.06	0.036	0.23 \pm 0.05	0.009	0.59 \pm 0.05	0.036	2.56 \pm 0.08	0.165
NGC5728	0.95 \pm 0.10	0.061	0.42 \pm 0.09	0.035	2.84 \pm 0.10	0.197	2.26 \pm 0.06	0.084	7.69 \pm 0.06	0.162	3.85 \pm 0.08	0.081	13.7 \pm 0.09	0.244	-	-	6.29 \pm 0.12	0.094	9.87 \pm 0.17	0.145
NGC7682	1.34 \pm 0.05	0.073	-	-	0.86 \pm 0.02	0.029	5.10 \pm 0.02	0.164	3.79 \pm 0.04	0.109	4.60 \pm 0.05	0.093	4.42 \pm 0.04	0.077	-	-	6.03 \pm 0.09	0.102	12.2 \pm 0.11	0.203